



Theoretical model of pediatric orbital trapdoor fractures and provisional personalized 3D printing-assisted surgical solution

Guangrui Chai^a, Deming Zhang^{b,d}, Weijian Hua^c, Jun Yin^d, Yifei Jin^c, Ming Chen^{a,*}

^a Department of Ophthalmology, Shengjing Hospital of China Medical University, Shenyang, Liaoning 110004, China

^b Department of Mechanical and Aerospace Engineering, University of Florida, Gainesville, FL 32611, USA

^c Department of Mechanical Engineering, University of Nevada Reno, Reno, NV, 89557, USA

^d The State Key Laboratory of Fluid Power and Mechatronic Systems, School of Mechanical Engineering, Zhejiang University, Hangzhou, Zhejiang 310027, China

ARTICLE INFO

Keywords:

Pediatric orbital fracture
Stress analysis
Trapdoor
3D printing
Personalized surgery

ABSTRACT

Pediatric orbital trapdoor fractures are common in children and adolescents and usually require emergency surgical intervention. Herein, a personalized 3D printing-assisted approach to surgical treatment is proposed, serving to accurately and effectively repair pediatric orbital trapdoor fractures. We first investigated stress distribution in external force-induced orbital blowout fractures via numerical simulation, determining that maximum stresses on inferior and medial walls exceed those on superior and lateral walls and thus confer higher probability of fracture. We also examined 36 pediatric patients treated for orbital trapdoor fractures between 2014 and 2019 to verify our theoretical construct. Using 3D printing technique, we then created orbital models based on computed tomography (CT) studies of these patients. Absorbable implants were tailor-made, replicating those of 3D-printed models during surgical repairs of fractured orbital bones. As follow-up, we compared CT images and clinical parameters (extraocular movements, diplopia, enophthalmos) before and 12 months after operative procedures. There were only two patients with diplopia and six with enophthalmos > 2 mm at 12 months, attesting to the efficacy of our novel 3D printing-assisted strategy.

1. Introduction

Trapdoor (or valve-like) orbital fractures are common in children. This particular type of orbital blowout fracture involves simple fracture of inferior wall, medial wall, or both, although inferior orbital wall is most often affected [1]. Because youthful bones are more elastic than adult bones, the fractured segments readily rebound after injury, trapping herniated intraorbital soft tissues along the edges and producing tell-tale manifestations (i.e. ocular motility restriction, diplopia, nausea, or vomiting). Reparative surgery is thus highly advised once such fractures occur.

In traditional surgical procedures, absorbable implants are trimmed into desired shapes, relying largely on a surgeon's expertise. There is limited operative exposure for this purpose. Surgeons generally resort to trial and error, gradually forming suitable implants. This practice is time-consuming and tedious, prolonging reparative procedures and aggravating postoperative edema [2]. Given the vital nerves, blood vessels, muscles, glands, and fat deposits indigenous to orbital regions, it becomes a major challenge to accurately repair orbital fractures and

effectively reduce collateral injuries if implant shapes do not match the fractured areas [3]. A new approach is therefore needed to permit rapid shaping and accurate trimming of absorbable implants.

The introduction of 3D printing technology has unleashed a powerful tool for on-demand high-precision presurgical modeling, representing a complete departure from traditional fracture repair. Physiologic data on fracture locations are extracted from computed tomography (CT) scans and reconstructed into virtual 3D models using computer-aided design (CAD) software. Various 3D printing techniques are then engaged to fabricate custom 3D fracture models, from which suitable implants are easily rendered. Not only is implant preparation time significantly reduced, but the accuracy of shaped implants is also markedly improved. 3D printing-assisted surgical treatments have been widely used in clinical studies to more reliably perform orbital reconstruction [4–9].

In the present study, numerical simulation was first conducted to analyze stress during external force-induced orbital blowout fractures and explore the probabilities attached to various fracture scenarios. Children treated for orbital trapdoor fractures were then studied in

Peer review under responsibility of KeAi Communications Co., Ltd.

* Corresponding author.

E-mail address: chenming@sj-hospital.org (M. Chen).

<https://doi.org/10.1016/j.bioactmat.2020.08.029>

Received 13 May 2020; Received in revised form 9 August 2020; Accepted 31 August 2020

2452-199X/© 2020 The Authors. Publishing services by Elsevier B.V. on behalf of KeAi Communications Co., Ltd. This is an open access article under the CC BY-NC-ND license (<http://creativecommons.org/licenses/by-nc-nd/4.0/>).

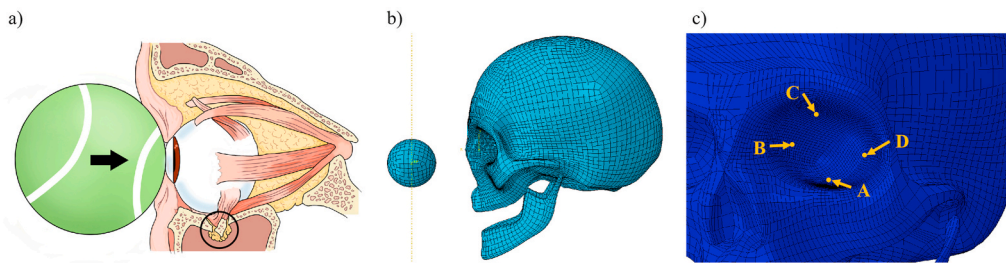


Fig. 1. Modeling of tennis ball impact-induced orbital blowout fracture: (a) schematic of tennis ball impact-induced orbital fracture; (b) meshed 3D model of tennis ball-human skull system; and (c) four-point site-specific evaluation of orbital bones.

retrospect to verify our theoretical construct. Thereafter, a personalized 3D printing-assisted surgical strategy was devised to create absorbable implants and repair fractured orbital bones. The feasibility and superiority of this novel approach were ultimately validated through follow-up clinical monitoring.

2. Numerical simulation

2.1. Modeling of tennis ball impact-induced orbital blowout fractures

External force, as in falls, traffic accidents, impact sports, or violence, is primarily responsible for orbital blowout fractures. Impact injury by a ball is one of the most common events in sports and served as an example in our investigation of pediatric orbital trapdoor fractures. We used the transmission theory to describe fracture mechanisms during impact. When an object, such as a tennis ball, strikes the orbital area, the transfer of impact force to orbital bones is multidirectional and may result in orbital fracture if maximum stress exceeds fracture stress in a particular bone, as shown in Fig. 1(a). The effects of eyeballs and soft tissues, such as muscles and orbital fat, on force transmission were ignored to simplify the model and improve convergence. For analysis of orbital stress generated accordingly, we used numerical simulation.

Tennis ball and skull models were first created in SolidWorks (Dassault Systèmes SolidWorks Corp, Waltham, MA, USA) and imported into a commercial finite element software package (ABAQUS v6.13; Dassault Systèmes Simulia Corp, Johnston, RI, USA) for meshing, as shown in Fig. 1(b). Although orbital anatomy may differ by age, most of our subjects were 7–11 years old. Our pediatric skull model was subsequently based on CT data from a typical 10-year-old patient. The Mooney-Rivlin model, best suited for tennis ball hyperelasticity, was used to describe material properties [10–14] as follows:

$$U = C_{10}(\bar{I}_1 - 3) + C_{01}(\bar{I}_2 - 3) + \frac{1}{D_1}(J^{el} - 1)^2$$

where U is strain energy density; C_{10} (=0.69 MPa), C_{01} (=0.17 MPa), and D_1 (=0.0145 MPa⁻¹) are material constants; J^{el} is elastic volume ratio; and \bar{I}_1 and \bar{I}_2 are first and second deviatoric strain invariants, respectively.

Many researchers have applied the Johnson-Cook equation to successfully model the mechanical properties of bone in the human skull [15–18]. This was selected as the constitutive model to describe non-elastic behavior of skull as follows:

$$\sigma = (A + B\varepsilon^n)(1 + C \ln \dot{\varepsilon}^*)(1 - T^{*m})$$

where σ is stress and A (=50 MPa), B (=101 MPa), C (=0.03), n (=0.08), and m (=0) are material-related constants. Because pediatric bones are more flexible and less brittle than adult bones, all aforementioned material-related constants were corrected by a factor of 0.66 [19] to accurately mimic mechanical properties of the pediatric skull (ε being equivalent plastic strain, $\dot{\varepsilon}^*$ and T^* denoting normalized strain rate and temperature, respectively), which were calculated as follows:

$$\dot{\varepsilon}^* = \frac{\dot{\varepsilon}}{\dot{\varepsilon}_0} \text{ and } T^* = \frac{T - T_0}{T_m - T_0}, \text{ where } \dot{\varepsilon} \text{ is plastic strain rate; } \dot{\varepsilon}_0 \text{ is effective}$$

plastic strain rate of the quasi-static test used to determine yield and hardening parameters A , B , and n ; T is temperature; and T_0 and T_m are reference temperature and reference melt temperature, respectively.

To evaluate stress distribution throughout the orbital region, four points situated on inferior wall (A), medial wall (B), superior wall (C), and lateral wall (D) were designated, as shown in Fig. 1(c). During tennis ball impact, we analyzed changes in stress at these four points. Except for parameters cited in the literature (enclosed in parentheses), other key settings for simulation were as follows: radius of tennis ball, 20 mm; initial internal pressure of tennis ball, ~41 KPa; velocity of tennis ball before impact, 6–7 m/s; density of tennis ball, 1068 kg/m³; skull modulus, 20 GPa; Poisson's ratio for skull, 0.36; and ambient atmospheric pressure, 100 KPa.

2.2. Simulation results and discussion

Simulation results are detailed in Fig. 2. As shown in Fig. 2(a), stress at each point peaked within a very short time (~0.01 s) during tennis ball impact and gradually diminished, although each point reached maximum stress at different times. Points A and B reached maximum stresses almost simultaneously (~0.006 s), as indicated in Fig. 2(a). However, maximum stress at point A (46.01 MPa) was slightly higher than that at point B (41.84 MPa), as indicated in Fig. 2(b). Maximum stress at point C (~32.42 MPa), reached 0.009 s after impact and shown in Fig. 2(c), was surpassed by values at points A and B but exceeded the maximum stress at point D (27.22 MPa), as indicated in Fig. 2(d). Stress distributions at the four selected points were thus characterized as follows:

$$\sigma_{\max,A} > \sigma_{\max,B} \gg \sigma_{\max,C} > \sigma_{\max,D} \quad \text{and} \quad t_{\max,A} = t_{\max,B} < t_{\max,D} < t_{\max,C}.$$

Points A and B sustained the greatest stress immediately after impact, resulting in higher risk of fracture. In theory at least, the probability of orbital blowout fracture appears to be ordered as follows: inferior wall > medial wall > superior wall > lateral wall. Hydraulic theory is another means of exploring orbital blowout fractures that will be tested in a numerical model going forward, assessing the transfer of impact force to orbital bones via eyeballs and soft tissues. Once added to the above model, the mechanisms of orbital blowout fractures may be better understood.

3. Retrospective case study

To verify our tentative hierarchy of site-specific fracture probabilities, 36 pediatric patients (male, 22; female, 14) with unilateral orbital fractures were selected for study, their ages ranging from 3 to 15 years. All patients were treated by ophthalmologists at Shengjing Hospital of China Medical University, undergoing surgical repairs of orbital trapdoor fractures between 2014 and 2019. The study protocol adhered to tenets in the Declaration of Helsinki and was approved by the Ethics Committee of Shengjing Hospital. Trapdoor fractures were diagnosed by preoperative CT scans and patient examinations, assessing extraocular movements and checking for diplopia. Detailed patient information is provided in Table 1.

We found that the vast majority of fractures (31/36) involved inferior orbital wall, fractures of medial orbital wall accounting for the

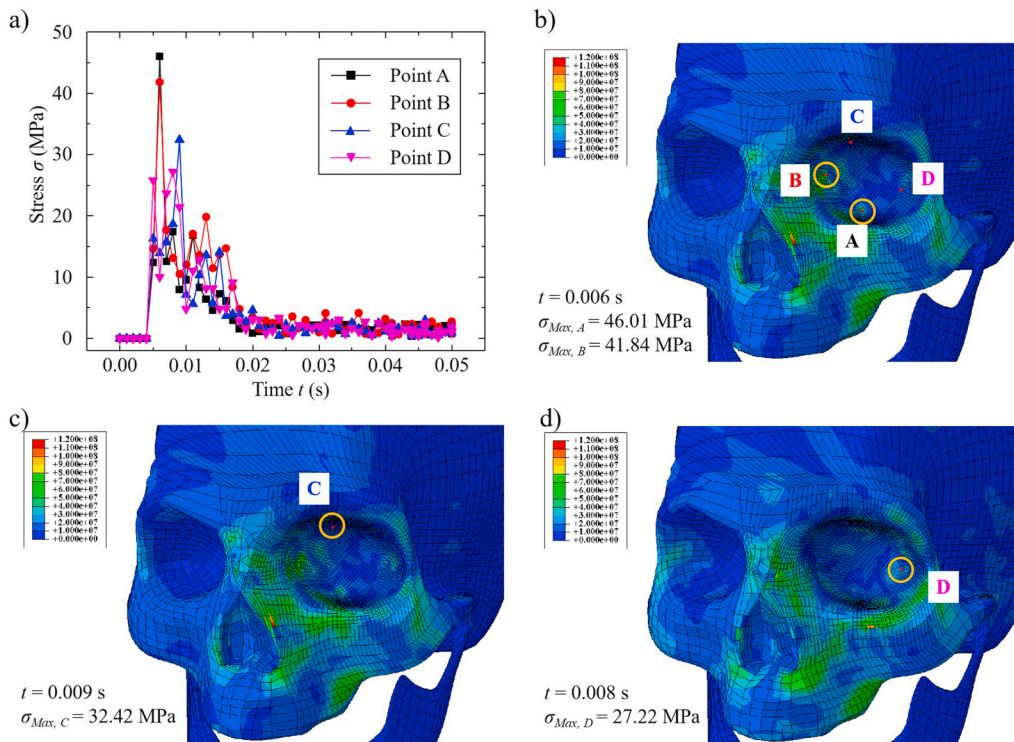


Fig. 2. Results of tennis ball impact simulation: (a) stress as a function of impact time at four specified points; and maximum stress distribution at (b) points A and B, (c) point C, and (d) point D.

Table 1
Patients' demographics.

Characteristics	Number (%)
Gender	
Male	22 (61.1%)
Female	14 (38.9%)
Age (year)	
< 5	3 (8.3%)
5–10	21 (58.3%)
> 10	12 (33.4%)
Fracture causes	
Fall	10 (27.8%)
Traffic accidents	8 (22.2%)
Impact in sports	8 (22.2%)
Violence	6 (16.7%)
Others	4 (11.1%)
Symptoms	
Nausea/vomiting	25 (69.4%)
Headache	10 (27.8%)
Diplopia	35 (97.2%)
Fracture location	
Inferior wall	31 (86.1%)
Medial wall	5 (15.9%)
Surgery time (hour)	
< 24	7 (19.4%)
24–72	17 (47.2%)
> 72	12 (33.4%)

rest (5/36). This data is consistent with fracture probabilities predicted through simulation. Although tennis ball impact was implicated in just 22.2% of such fractures, our simulation results may be extrapolated to all 36 patients and to other events associated with external force-induced fracture, such as falls, traffic accidents, and violence. The

distribution of fractures in all 36 patients is shown according to the causes in Table 1. Regardless of its basis (i.e. a 10-year-old pediatric skull model), results of the simulation may be used to predict fracture locations across all ages (3–15 years old), thus validating the general applicability of the simulation results.

4. Personalized 3D printing-assisted surgical approach

4.1. Preoperative preparation

3D CT scans were performed horizontally, coronally, and sagittally in each patient immediately after injury. The scanning parameters applied were as follows: slice thickness, 1.00 mm; pixel matrix, 512×512 ; working voltage, 120 kV; current, 225 mA; window width, 2000 HU; and window level, 400 HU.

We imported original CT imaging data into an open-source software application (3D Slicer) for analysis and to create virtual models of orbital fracture. The models were saved as stereolithography (STL) files and imported into a commercial 3D printer (MakerBot Replicator 2; MakerBot Industries LLC, Brooklyn, NY, USA). Polylactic acid (PLA) fibers (MP05823; MakerBot Industries) served as the build material, were used to generate polymeric melts in the print head at a working temperature above the melting point. Melts were then extruded as continuous filaments through the printing nozzle tip. Ambient temperature (i.e. room temperature) was much lower than the melting temperature, allowing extruded filaments to rapidly solidify. Each 3D orbital fracture model was thereby printed in layered fashion. To limit the time invested, only fractured sections and abutments needed for surgery were obtained, usually in ~1–1.5 h (depending on inherent complexities). Completed orbital fracture models were sent to the operating room and sterilized (ethylene oxide) in advance of surgery. Key dimensions of 3D models were monitored before and after sterilization and did not measurably change, underscoring their shape stability. Figs. 3(a-1) and 3 (b-1) show virtual models of inferior and medial orbital wall fractures, respectively, with corresponding surgeries

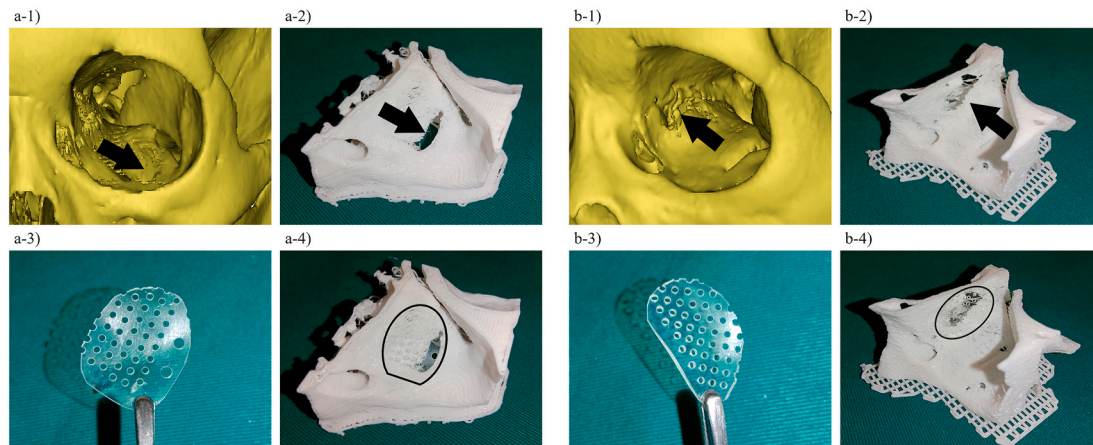


Fig. 3. Virtual models of orbital fracture at (a-1) inferior wall and at (b-1) medial wall; 3D-printed orbital fracture models for (a-2) inferior wall and (b-2) medial wall; and trimmed/shaped absorbable implants for surgical repair of (a-3, a-4) inferior wall fracture and (b-3, b-4) medial wall fracture.

depicted in Figs. 3(a-2) and 3 (b-2). Orbital wall fractures are indicated by black arrows.

4.2. Surgical methods

All surgeries were performed under general anesthesia. Forced duction testing was conducted to determine if restricted motion persisted once administered. In patients with inferior wall fractures, lower eyelid conjunctiva was incised, completely exposing orbital wall and fracture edge. For medial wall fractures, entry was through conjunctiva of lacrimal caruncle. All orbital soft tissues entrapped in sinuses (maxillary and ethmoid) were fully released and returned to the orbit. In those patients with entrapped extraocular muscles (inferior and medial rectus), fracture areas were enlarged along the breaks in order to reset them and avoid collateral injuries. Depending on injuries sustained, absorbable mesh plates (PLLA/PGA 85:15, RapidSorb OrbFloor Plate 1.5 or 0.5 mm; DePuy Synthes, Raynham, MA, USA) were soaked in aseptic saline at 90 °C for softening and shaping on printed models. Once these plates hardened (at room temperature), they were trimmed to form precise fracture overlays, without compromising surrounding infraorbital nerves. Implants for repairing inferior and medial wall fractures are illustrated in Figs. 3(a-3)/3 (a-4) and 3(b-3)/3(b-4), respectively. After use of a brain pressure plate to completely expose fractured areas, the implants were mounted to bones by tissue glue. Passive traction testing of the dried implants was done to exclude potential incarceration and ensure unconstrained eyeball rotation. Finally, intermittent absorbable suturing (model: 6-0) was undertaken for conjunctival closure. The surgically repaired eyes were smeared with antibiotic eye ointment and bandaged under pressure for 1 day.

4.3. Postsurgical follow-up

On the first postoperative day, visual acuity and ocular motility were examined in the morning. Intravenous drips of antibiotics were routinely initiated on days of surgery and continued for 2 days afterwards. Patients were discharged from the hospital 3–5 days after surgery and monitored during return visits at 1 week, 1 month, 3 months, 6 months, and 12 months after surgery. Ocular motility, diplopia, and degree of enophthalmos were measures of patient recovery. Those patients with restricted ocular motility and diplopia at postoperative Week 1 were instructed on rehabilitative training of eye movements, to be performed twice daily for 45 min. Those with inferior wall fractures were tasked with reciprocating eye movement in vertical plane. The same movements in horizontal plane were required for medial wall fractures. 3D CT scans of the orbit were obtained 3 days and 12 months postoperatively to assess surgical repairs. The primary gauge of patient

recovery was enophthalmos, which was measured as follows: 1) CT imaging data were collected in follow-up 12 months after surgery, rotating axial CT images in 3D Slicer software; 2) images incorporating the largest sections of lens aligned with optic canal were selected for measurements; 3) lateral orbital edges were connected to establish baselines, and vertical lines were drawn from highest corneal points to these baselines; and 4) the measured vertical lines indicated degree (mm) of eyeball protrusion. Three determinations were made, recording the average as postoperative persistence of enophthalmos. A single example is illustrated in Fig. 4.

5. Outcomes and discussion

5.1. Surgical results

Using our personalized 3D printing-assisted surgical strategy, all patients displayed excellent anatomic reductions 3 days after surgery in CT studies. Results in one representative patient are illustrated in Fig. 5, comparing images before and after inferior wall fracture repair. Figs. 5(a-1) through 5 (a-3) show CT views of the left-sided fracture. Upward and downward constraints on extraocular movements are demonstrated in Figs. 5(a-4) and 5 (a-5). CT images of the same patient 3 days after surgery, seen in Figs. 5(b-1) through 5 (b-3), indicate that absorbable implants effectively repaired the fracture, confirmed by normal and smooth left eye movement in Figs. 5(b-4) and 5 (b-5).

Results in another representative patient with medial wall fracture are illustrated in Fig. 6. CT images in Figs. 6(a-1) and 6 (a-2), obtained preoperatively, are contrasted with Figs. 6(b-1) and 6 (b-2), showing effective repair of the fractured orbit through 3D printing-assisted surgery. Before operative treatment, inner rotation of the left eye was



Fig. 4. Gauging of postoperative exophthalmos.

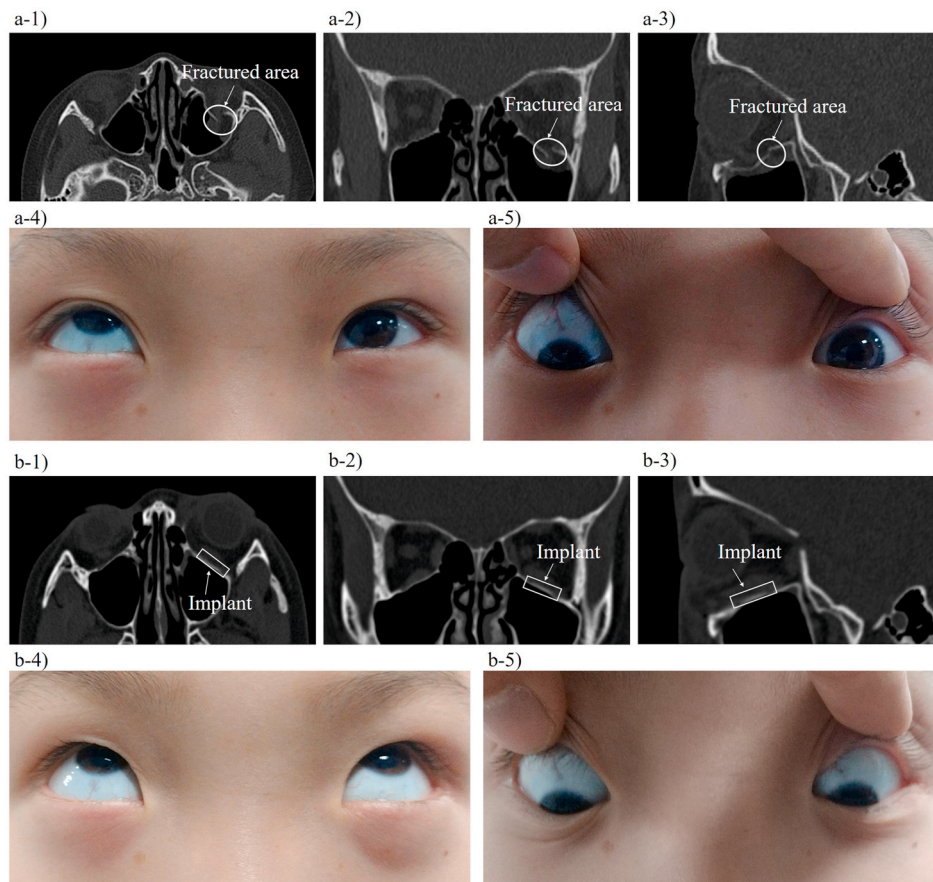


Fig. 5. CT images obtained (a-1 through a-3) before and (b-1 through b-3) after surgical repair of inferior wall fracture; and outcomes of extraocular muscle (EOM) examinations conducted (a-4, a-5) before and (b-4, b-5) after surgery.

limited, as Figs. 6(a-3) and 6 (a-4) indicate, although this has been resolved in Figs. 6(b-3) and 6 (b-4), after surgical repair.

Follow-up data, checking for postoperative diplopia and enophthalmos in all 36 patients, are summarized in Table 2. There were only two patients with diplopia and six showing enophthalmos > 2 mm at 12 months after surgery, attesting to the efficacy of our personalized 3D printing-assisted surgical strategy.

5.2. Discussion

A trapdoor fracture is the most common type of orbital fracture in children, marked by negligible displacement of affected bones. In 1998, Jordan et al. performed an in-depth study of such injuries for the first time [20], suggesting the term “white-eyed blowout fracture” due to the absence of swelling or congestion in many patients. These are linear fractures of orbital walls caused by acute transient upsurges in orbital pressure. The fractured flap rebounds after initial outward split, regaining its original position at once. In doing so, periorbital soft tissues along lines of fracture may easily become entrapped, and ocular motility restriction becomes a potential hazard. This type of fracture is highly contingent on adequate bone elasticity, a characteristic of children's bones. The proportion of osteoblasts in children's bones is generally much greater than that of osteoclasts. Their bones are subsequently less calcific or brittle and far more flexible [21]. In contrast, adults are prone to comminuted fractures due to progressive bony brittleness and declining elasticity [22]. Moreover, both ethmoidal and maxillary sinuses of children and adolescents are diminutive by comparison, leaving insufficient space for displacement and further encouraging a trapdoor configuration [23]. As a result, such fractures occur almost exclusively in children and adolescents.

From an engineering perspective, fracture occurs if localized maximum stress exceeds fracture strength. However, points of fracture also depend on certain anatomic factors, such as supporting tissues/bones (i.e. thin bones in ethmoidal labyrinth) bordering the orbits and the thickness of orbital bone itself. Both inferior and medial orbital walls are relatively thin (tenths of millimeters), more than superior and lateral walls (few to tens of millimeters), as shown in a number of patients. This disparity predisposes the inferior and medial walls to concentrated stress, heightening the probability of blowout at these two sites. In most individuals, the inferior wall is slightly thinner than medial wall. However, some patients may differ in this regard, given the complexities of human bodies. Medial wall fracture is also feasible during a ball impact. There were five patients with medial wall fractures among the 36 patients selected.

In this particular study, numerical simulation was invoked to analyze stress distribution and changes during external force-induced impact. We determined that frontal impact force may be transferred into the orbit, leading to dramatic spikes in intraorbital pressure and differing stress distributions on orbital walls. The inferior and medial orbital walls incur much higher maximum stress levels during impact injuries, further explaining the high risk of blowout in these two areas.

Nausea and vomiting are the most common symptoms of trapdoor fractures [24]. Herniated tissues entrapped by extraorbital muscles may incite vagal stimulation and trigger the oculocardiac reflex, creating a false impression of neurosurgical disease. These symptoms may render children uncooperative during physical examinations [25]. Areas of fracture are likewise apt to be relatively small or negligible in CT images, subject to misdiagnosed by less experienced ophthalmologists. In addition to nausea and vomiting, symptoms of pediatric orbital trapdoor fractures include vertical or horizontal diplopia, ocular

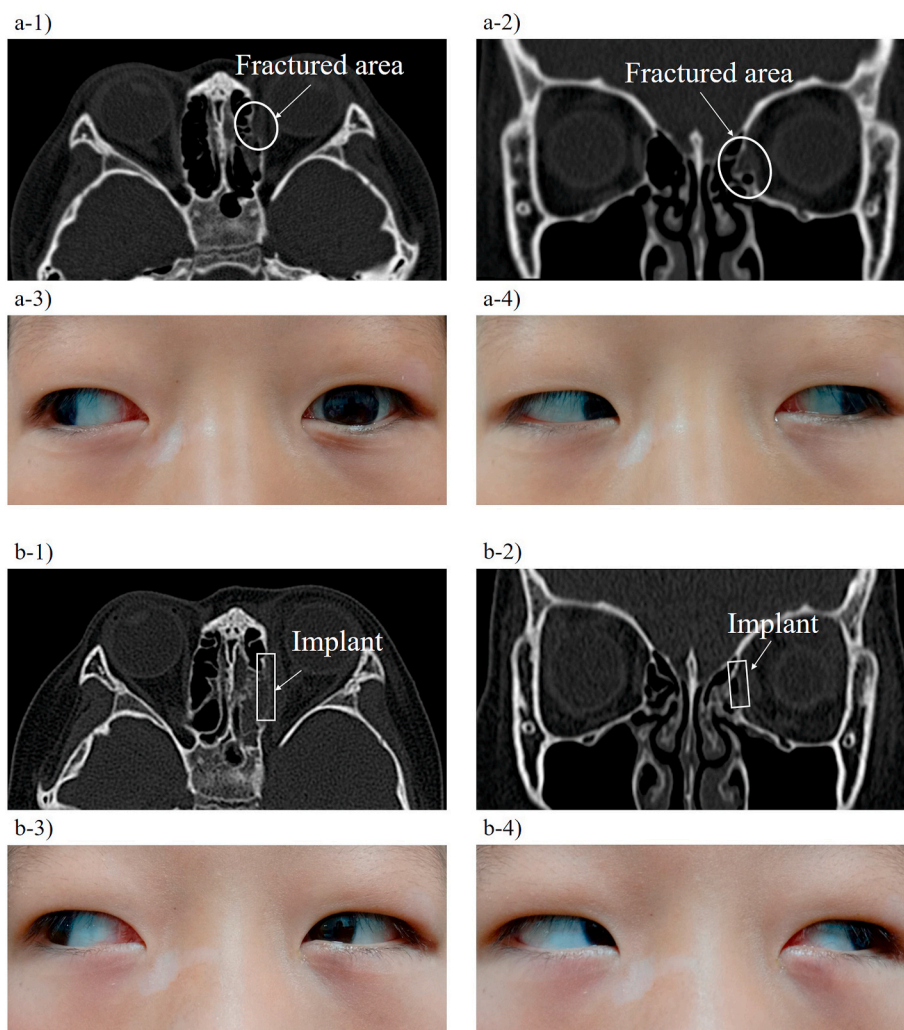


Fig. 6. CT images obtained (a-1, a-2) before and (b-1, b-2) after surgical repair of medial wall fracture; and outcomes of extraocular muscle (EOM) examinations conducted (a-3, a-4) before and (b-3, b-4) after surgery.

motility restriction, and severe pain with eye movement. Fractures of inferior orbital wall may well affect the infraorbital nerve, impairing sensation within ipsilateral upper cheek, upper jaw, and upper lip. In patients with linear fractures and no eye movement constraints or diplopia, CT evidence of muscle entrapment and soft tissue herniation is unlikely. Conservative treatment may therefore suffice, although follow-up monitoring is essential to ensure continued improvement and rule out late-developing enophthalmos [26].

Prompt surgical intervention is generally advised once trapdoor fractures occur. Based on time elapsed after point of injury, surgeries are categorized as emergency (within 24 h), early (24–96 h), or late (96 h later) procedures [27]. In short order, entrapped orbital tissue may become ischemic or necrotic, destined for prolonged atrophy. Consequently, trapdoor fracture is one of the rare facial fractures requiring emergency surgery [28]. In instances of extraocular muscle entrapment, it is best to perform surgery within 48 h. Delayed surgical

treatment may lead to the longer recovery time and worsen the prognosis [29].

Our personalized 3D printing-assisted surgical approach effectively reduced operative times on average and improved patient outcomes. A total of 21 pediatric patients with orbital fractures were analyzed in retrospect, each treated by ophthalmologists at Shengjing Hospital of China Medical University between 2009 and 2013. For comparison, operative times and complications of traditional and 3D printing-assisted surgical methods are summarized in Table 3. Traditional procedures performed prior to 2014 usually involved trial and error when trimming and shaping absorbable implant materials. Laborious handling of this sort extended the average operative time to ~90 min. However, the 3D printing-assisted method enabled clear fracture delineation in advance of surgery, allowing accurate trimming of implants during reparative procedures. This reduced the average operative time to just 45 min.

Table 2
Symptoms in the post-surgery follow-ups.

Postoperative follow-up time	1-week	1-month	3-month	6-month	12-month
Ocular motility restriction (N/T)	10/36	7/36	3/36	2/36	0/36
Diplopia (N/T)	15/36	12/36	5/36	3/36	2/36
Enophthalmos (> 2 mm) (N/T)	0/36	0/36	1/36	3/36	6/36

N: number of patients who have the symptom; T: total number of patients in follow-up.

Table 3
Comparison between patients treated by different surgical methods.

	Traditional method (2009–2013)	3D printing-assisted method (2014–2019)
Average operative time (minute)	90	45
Average hospitalization (day)	12	8
Time for reduction of swelling (week)	4	2
Diplopia at 12 months (N/T)	6/21	2/36
Enophthalmos over 2 mm at 12 months (N/T)	5/21	6/36

N: number of patients who have the symptom; T: total number of patients in follow-up.

Importantly, this new method of surgery effectively alleviates complications in treated patients. As shown in Table 3, the average time for reduction of swelling after 3D printing-assisted surgery was only 2 weeks, compared with ~4 weeks after traditional surgery; and average hospitalization was reduced from 12 days (for traditional surgery) to 8 days (for 3D printing-assisted surgery). After traditional procedures, diplopia was observed in 28.6% (6/21) of patients, and 23.8% (5/21) exhibited enophthalmos > 2 mm at 12 months. Corresponding rates for 3D printing-assisted surgeries were 5.6% (2/36) and 16.7% (6/36), thus validating the utility and efficacy of this strategy in repairing pediatric orbital fractures.

In our study population, we used transconjunctival access, rather than incising below the lash line or at inferior fornix, for the following reasons: 1) aesthetics are of greater concern in children and adolescents than in adults; 2) access via inferior fornix seems to encourage fatty herniation after orbital septum is damaged; and 3) postoperative valgus and hypertrophic scars due to improper access and suturing are largely avoided in this way [30].

Currently, a variety of implant materials, such as freeze-dried dura mater, polyethylene sheets, hydroxyapatite, autogenous bone, allogeneic bone, absorbable substances, and titanium mesh, are available for repair of orbital fractures in adults [31–33]. Implant choice is equally varied in children and adolescents, determined by product characteristics, fracture location, surgical convention, and other factors. Because orbital bone growth ceases at an early age (~16 years) in human development [27], absorbable materials are strongly advocated for patients < 16 years old to limit orbital effects. Still, original bones should be maximally preserved when repairing these often small-sized fractures. The poor capacity for load bearing makes absorbable implants quite suitable in this setting. Most will gradually biodegrade following surgery and will not affect the developing orbit [34].

Absorbable materials formulated for orbital fracture repair include polyester urane [35], poly-L/DL-lactide [36,37], poly-L-lactide [38,39], and poly-L-lactic acid-polyglycolic acid (PLLA-PGA) [40–42]. We opted for PLLA-PGA implants, given their unique properties. Compared with polyester urane (used exclusively to repair orbital floor after pediatric orbital trapdoor fractures) [35], PLLA-PGA has better mechanical stiffness/stability at room and physiologic temperatures, offering sufficient support during regeneration of both inferior and medial wall fractures. Its exceptional plasticity at higher temperatures (70–90 °C) also facilitates the shaping of implants to meet the needs of each patient. As a result, PLLA-PGA has been widely used to repair orbital trapdoor fractures in children [41,42]. In keeping with other reports, we used material with PLLA:PGA ratios of 85:15 for bony repairs [43]. A trimmed implant changes little within the first 2 months (4 weeks: 95% strength; 8 weeks, 85% strength) but is fully resorbed by 12 months [34], conforming perfectly with growth and regeneration periods in pediatric bones. In CT images obtained 12 months postoperatively, no absorbable implants were retained.

Some studies have shown a lack of significant correlation between severity of preoperative ocular motility restriction and time required for full postoperative recovery [44]. Preoperative ocular magnetic resonance imaging may be used to better define morphologic changes in extraocular muscles, gauge the extent of their injury, and further assess patient prognosis. However, forced duction testing and postoperative

rehabilitation training are pivotal for prognostication in patients with trapdoor fractures. Forced duction testing conducted prior to surgery may help distinguish ocular motility restriction from mechanical restriction or from extraocular muscle paralysis. After surgery, such testing may indicate whether entrapment is resolved or signal soft tissue retention between implants and orbital bones. According to reports, a combination of forced duction testing and 1 week of postoperative training provides substantial insight into patient prognosis [30].

Postoperative diplopia typically has two causes: 1) persistent trapping of atretic or herniated muscles and tissues, and 2) faulty shaping or placement of implants. In the first scenario, the fracture edge should be checked posteriorly to affirm that clamped muscles and tissues are completely released. Fracture areas and shapes may vary according to type of injury and patient physique. The extent to which implants and areas of fracture are matched will directly impact surgical results. Regardless of which implant material is used, dissecting and repairing orbital bones is necessary for resolution of enophthalmos and diplopia. In follow-up monitoring, we identified six patients with enophthalmos > 2 mm at postoperative Month 12. Past research suggests that this is likely due to intraorbital fat necrosis and atrophy [45]. Tissue that becomes trapped during pediatric orbital trapdoor fractures is predisposed to obverse necrosis or orbital fat atrophy.

The prognosis is excellent in most children with these injuries if surgical timing, methods, and implant materials are properly chosen. Nevertheless, patients may be slow to recover. Two of our subjects experienced similar outcomes. Although postoperative ocular motility restrictions had visibly resolved within 1 week, paralysis and contracture of inferior rectus muscle ensued by the second week, causing ocular motility restriction for 3 months. As recovery periods progressed, the affected muscles gradually softened and regained their elasticity, and normal ocular motility returned. Unexpected setbacks of this sort are always frustrating for surgeons.

6. Conclusions and future efforts

Given current advancements in personalized precision healthcare, patients now have heightened expectations for ophthalmologic surgery. Unfortunately, the complex anatomy and rich physiology of the orbit are problematic when using traditional surgical procedures for orbital fracture repair. Features gleaned through CT images and intraoperative visual inspection often fall short, making the trimming of implants a tenuous feat. Mismatch between implants and fractures may then lead to various complications [46]. However, 3D printing technology is a powerful tool for personalized repairs, offering tangible models of fracture sites. These tailor-made models facilitate the shaping of implants during surgery to precisely replicate fractured areas. Operative times are significantly reduced as a result.

The findings of this study may be summarized as follows:

1. Based on numerical simulation of related stresses, it appears that inferior and medial orbital walls are most susceptible to fracture. This principle reflects anatomic characteristics and is supported by retrospective case study;
2. 3D printing technique may help personalized absorbable implants,

enabling precision matches with fractured areas; and

- In 36 pediatric patients, orbital trapdoor fractures were successfully repaired using the personalized 3D printing-assisted surgical method that we have proposed.

Future investigative efforts may perhaps focus on direct 3D printing of absorbable implants using biocompatible and biodegradable polymers or polymer composites. The trimming of mesh plates into implants will then be unnecessary. Custom 3D implants that are printed prior to surgery, based on CT imaging data, enhance the structural accuracy of implants and reduce operative times. A broader sampling of pediatric patients from other hospitals must also be analyzed to validate our numerical simulation results and corroborate the efficacy of this personalized 3D printing-assisted surgical approach. The methodology we have adopted holds promise in the modeling of many fractures or fracture-related issues. Affected preschoolers (3–5 years old), adults, or patients with non-trap door fractures may be similarly addressed, exploring changes in stress variance and distribution as implants degrade after surgery.

CRedit authorship contribution statement

Guangrui Chai: Conceptualization, Formal analysis, conceived the concept of this work, performed all experiments, surgeries, and retrospective analysis, wrote the manuscript together. **Deming Zhang:** Formal analysis, conducted the numerical simulations and analysis, wrote the manuscript together. **Weijian Hua:** Formal analysis, conducted the numerical simulations and analysis, wrote the manuscript together. **Jun Yin:** Formal analysis, conducted the numerical simulations and analysis, wrote the manuscript together. **Yifei Jin:** Formal analysis, conducted the numerical simulations and analysis, wrote the manuscript together. **Ming Chen:** Formal analysis, performed all experiments, surgeries, and retrospective analysis, wrote the manuscript together, conceived the concept of this work.

Declaration of competing interest

The paper has not been published previously, that is not under consideration for publication elsewhere, and that if accepted it will not be published elsewhere in the same form, in English or in any other languages, without the written consent of the publisher.

References

- A.F. Miller, D.M. Elman, P.L. Aronson, A.A. Kimia, M.I. Neuman, Epidemiology and predictors of orbital fractures in children, *Pediatr. Emerg. Care* 34 (2018) 21–24 <https://doi/10.1097/PEC.0000000000001306>.
- S. Grob, M. Yonkers, J. Tao, Orbital fracture repair, *Semin. Plast. Surg.* 31 (2017) 31–39 <https://doi/10.1055/s-0037-1598191>.
- C.T. Chen, Y.R. Chen, Update on orbital reconstruction, *Curr. Opin. Otolaryngol. Head Neck Surg.* 18 (2010) 311–316 <https://doi/10.1097/MOO.0b013e328333aafd2>.
- M. Vehmeijer, M. van Eijnatten, N. Liberton, J. Wolff, A novel method of orbital floor reconstruction using virtual planning, 3-dimensional printing, and autologous bone, *J. Oral Maxillofac. Surg.* 74 (2016) 1608–1612 <https://doi/10.1016/j.joms.2016.03.044>.
- S.W. Park, J.W. Choi, K.S. Koh, T.S. Oh, Mirror-imaged rapid prototype skull model and pre-molded synthetic scaffold to achieve optimal orbital cavity reconstruction, *J. Oral Maxillofac. Surg.* 73 (2015) 1540–1553 <https://doi/10.1016/j.joms.2015.03.025>.
- T.S. Oh, W.S. Jeong, T.J. Chang, K.S. Koh, J.W. Choi, Customized orbital wall reconstruction using three-dimensionally printed rapid prototype model in patients with orbital wall fracture, *J. Craniofac. Surg.* 27 (2016) 2020–2024 <https://doi/10.1097/SCS.0000000000003195>.
- A.B. Callahan, A.A. Campbell, C. Petris, M. Kazim, Low-cost 3D printing orbital implant templates in secondary orbital reconstructions, *Ophthalmic Plast. Reconstr. Surg.* 33 (2017) 376–380 <https://doi/10.1097/IOP.0000000000000884>.
- R. Zielinski, M. Malinska, M. Kozakiewicz, Classical versus custom orbital wall reconstruction: selected factors regarding surgery and hospitalization, *J. Cranio-Maxillo-Fac. Surg.* 45 (2017) 710–715 <https://doi/10.1016/j.jcms.2017.02.008>.
- B. Fan, H. Chen, Y.J. Sun, B.F. Wang, L. Che, S.Y. Liu, G.Y. Li, Clinical effects of 3-D printing-assisted personalized reconstructive surgery for blowout orbital fractures, *Graefes Arch. Clin. Exp. Ophthalmol.* 255 (2017) 2051–2057 <https://doi/10.1007/s00417-017-3766-y>.
- R. Hambli, A. Chamekh, H.B.H. Salah, Real-time deformation of structure using finite element and Neural networks in virtual reality applications, *Finite Elem. Anal. Des.* 42 (2006) 985–991 <https://doi/10.1016/j.finel.2006.03.008>.
- C.W. Macosko, *Rheology: Principles, Measurement and Applications*, Wiley-VCH Publishers, New York, USA, 1994.
- Y.S. Kim, Y.J. Zhang, M.K. Bae, M.S. Kim, A-13 FEM Analyses for Dynamic Characteristics of Tennis Racket and Ball Using Interlaced Solid String Model, *The Japan Society of Mechanical Engineers*, 2009, pp. 66–71 <https://doi/10.1299/jsmesports.2009.0.66>.
- L. Li, S.H. Yang, C.S. Hwang, Y.S. Kim, Effects of string tension and impact location on tennis playing, *J. Mech. Sci. Technol.* 23 (2009) 2990–2997 <https://doi/10.1007/s12206-009-0903-5>.
- K. Alireza, K. Susumu, R. Reza, N. Mahdi, Measurement of the mechanical properties of the handball, volleyball, and basketball using DIC method: a combination of experimental, constitutive, and viscoelastic models, *J Sport Health Sci* 11 (2015) 295–303 <https://doi/10.1007/s11332-015-0240-2>.
- K. Alam, A.V. Mitrofanov, V.V. Silberschmidt, Thermal analysis of orthogonal cutting of cortical bone using finite element simulations, *Int. J. Exp. Comput. BioMech.* 3 (2010) 236–251 <https://doi/10.1504/IJECB.2010.035259>.
- C. Santuste, M. Rodriguez-Millan, E. Giner, H. Migulez, The influence of anisotropy in numerical modeling of orthogonal cutting of cortical bone, *Compos. Struct.* 116 (2014) 423–431 <https://doi/10.1016/j.compstruct.2014.05.031>.
- K. Alam, A.V. Mitrofanov, V.V. Silberschmidt, Finite element analysis of forces of plane cutting of cortical bone, *Comput. Mater. Sci.* 46 (2009) 738–743 <https://doi/10.1016/j.commatsci.2009.04.035>.
- A. Garo, P.J. Arnoux, C.E. Aubin, Estimation of bone material properties using an inverse finite element method, *Comput Method Biomed* 12 (2009) 121–122 <https://doi/10.1080/10255840903080851>.
- Y. Meng, C.D. Untaroiu, A review of pediatric lower extremity data for pedestrian numerical modeling: injury epidemiology, anatomy, anthropometry, structural, and mechanical properties, *Appl. Bionics Biomechanics* 2018 (2018) 1–20 <https://doi/10.1155/2018/6271898>.
- D.R. Jordan, L.H. Allen, J. White, J. Harvey, R. Pashby, B. Esmaeli, Intervention within days for some orbital floor fractures: the white-eyed blowout, *Ophthalmic Plast. Reconstr. Surg.* 14 (1998) 379–390 <https://doi/10.1097/00002341-199811000-00001>.
- Y. Takahashi, M.S. Sabundayo, H. Miyazaki, H. Mito, H. Kakizaki, Orbital trapdoor fractures: different clinical profiles between adult and paediatric patients, *Br. J. Ophthalmol.* 102 (2018) 885–891 <https://doi/10.1136/bjophthalmol-2017-310890>.
- L.T. Phan, W. Jordan Piluek, T.J. McCulley, Orbital trapdoor fractures, *Saudi J Ophthalmol* 26 (2012) 277–282 <https://doi/10.1016/j.sjopt.2012.05.008>.
- J.H. Grant, J.R. Patrinely, A.H. Weiss, P.C. Kierney, J.S. Gruss, Trapdoor fracture of the orbit in a pediatric population, *Plast. Reconstr. Surg.* 109 (2002) 482–489 <https://doi/10.1097/00006534-200202000-00011>.
- S.H. Baek, E.Y. Lee, Clinical analysis of internal orbital fractures in children, *Kor. J. Ophthalmol.* 17 (2003) 44–49 <https://doi/10.3341/kjo.2003.17.1.44>.
- H.R. Lee, G.Y. Jung, D.L. Lee, H.K. Shin, Pediatric orbital medial wall trapdoor fracture with normal computed tomography findings, *Arch Craniofac Surg* 18 (2017) 128–131 <https://doi/10.7181/acs.2017.18.2.128>.
- S. Joshi, W. Kassira, S.R. Thaller, Overview of pediatric orbital fractures, *J. Craniofac. Surg.* 22 (2011) 1330–1332 <https://doi/10.1097/SCS.0b013e31821c9365>.
- G. Gerbino, F. Rocca, F.A. Bianchi, E. Zavattoni, Surgical management of orbital trapdoor fracture in a pediatric population, *J. Oral Maxillofac. Surg.* 68 (2010) 1310–1316 <https://doi/10.1016/j.joms.2009.12.037>.
- K. Maloney, Non-displaced pediatric orbital fracture with displacement of the inferior rectus muscle into the maxillary sinus: a case report and review of the literature, *Int. J. Oral Maxillofac. Surg.* 43 (2014) 29–31 <https://doi/10.1016/j.ijom.2013.04.021>.
- Y. Su, Q. Shen, X. Bi, M. Lin, X. Fan, Delayed surgical treatment of orbital trapdoor fracture in paediatric patients, *Br. J. Ophthalmol.* 103 (2019) 523–526 <https://doi/10.1136/bjophthalmol-2018-311954>.
- Y. Li, X. Song, L. Li, X. Fan, M. Lin, Forced duction training: a potential key point for recovery in pediatric patients with trapdoor fracture, *Medicine (Baltim.)* 95 (2016) e5121 <https://doi/10.1097/MD.0000000000005121>.
- F. Bano, Biomaterials and implants for orbital floor repair, *Acta Biomater.* 7 (2011) 3248–3266 <https://doi/10.1016/j.actbio.2011.05.016>.
- D.R. Gunarajah, N. Samman, Biomaterials for repair of orbital floor blowout fractures: a systematic review, *J. Oral Maxillofac. Surg.* 71 (2013) 550–570 <https://doi/10.1016/j.joms.2012.10.029>.
- S.J. Moon, H.S. Suh, B.Y. Park, S.R. Kang, Safety of silastic sheet for orbital wall reconstruction, *Arch Plast Surg* 41 (2014) 362–365 <https://doi/10.5999/aps.2014.41.4.362>.
- S. Ramesh, S. Subhshman, R. Goldberg, Resorbable implants for orbital fractures: a systematic review, *Ann. Plast. Surg.* 81 (2018) 372–379 <https://doi/10.1097/SAP.0000000000001504>.
- M. Abumanhal, R. Ben-Cnaan, I. Feldman, S. Keren, I. Leibovitch, Polyester urethane implants for orbital trapdoor fracture repair in children, *J. Oral Maxillofac. Surg.* 77 (2019) 126–131 <https://doi/10.1016/j.joms.2018.08.005>.
- J. Al-Sukhun, J. Tornwall, C. Lindqvist, R. Kontio, Bioresorbable poly-L/DL-lactide (P[L]/DL[LA] 70/30) plates are reliable for repairing large inferior orbital wall bony defects: a pilot study, *J. Oral Maxillofac. Surg.* 64 (2006) 47–55 <https://doi/10.1016/j.joms.2005.09.013>.

- [37] O. Lieger, B. Schaller, J. Zix, F. Kellner, T. Lizuka, Repair of orbital floor fractures using bioresorbable poly-L/DL-lactide plates, *Arch. Facial Plast. Surg.* 6 (2010) 399–404 <https://doi/10.1001/archfacial.2010.91>.
- [38] F.W. Cordewener, R.R. Bos, F.R. Rozema, W.A. Houtman, Poly(L-lactide) implants for repair of human orbital floor defects: clinical and magnetic resonance imaging evaluation of long-term results, *J. Oral Maxillofac. Surg.* 54 (1996) 9–13 [https://doi/10.1016/S0278-2391\(96\)90292-X](https://doi/10.1016/S0278-2391(96)90292-X).
- [39] E.J. Bergsma, F.R. Rozema, R.R. Bos, W.C. De Bruijn, Foreign body reactions to resorbable poly(L-lactide) bone plates and screws used for the fixation of unstable zygomatic fractures, *J. Oral Maxillofac. Surg.* 51 (1993) 666–670 [https://doi/10.1016/S0278-2391\(10\)80267-8](https://doi/10.1016/S0278-2391(10)80267-8).
- [40] B.L. Eppley, M. Reilly, Degradation characteristics of PLLA-PGA bone fixation devices, *J. Craniofac. Surg.* 8 (1997) 116–120 <https://doi/10.1097/00001665-199703000-00010>.
- [41] F.G. Magana, R.M. Arzac, L. De Hilario Aviles, Combined use of titanium mesh and resorbable PLLA-PGA implant in the treatment of large orbital floor fractures, *J. Craniofac. Surg.* 22 (2011) 1991–1995 <https://doi/10.1097/SCS.0b013e3182319615>.
- [42] B.L. Eppley, L. Morales, R. Wood, J. Pensler, J. Goldstein, R.J. Havlik, M. Habal, A. Losken, J.K. Williams, F. Burstein, A.A. Rozzelle, Resorbable PLLA-PGA plate and screw fixation in pediatric craniofacial surgery: clinical experience in 1883 patients, *Plast. Reconstr. Surg.* 114 (2004) 850–856 <https://doi/10.1097/01.PRS.0000132856.69391.43>.
- [43] O.F.S. Avilés, M.F.M. Mauledoux, G.M.R. Oscar, F.G.R. Hoffman, S.D. Max, FEA of bioabsorbable material to repair hand fractures, *Appl. Mech. Mater.* 823 (2016) 173–178 <https://doi/10.4028/www.scientific.net/AMM.823.173>.
- [44] J.W. Yang, J.E. Woo, J.H. An, Surgical outcomes of orbital trapdoor fracture in children and adolescents, *J. Cranio-Maxillo-Fac. Surg.* 43 (2015) 444–447 <https://doi/10.1016/j.jcms.2015.01.010>.
- [45] S.M. Kim, Y.S. Jeong, I.J. Lee, M.C. Park, D.H. Park, Prediction of the development of late enophthalmos in pure blowout fractures: delayed orbital tissue atrophy plays a major role, *Eur. J. Ophthalmol.* 27 (2017) 104–108 <https://doi/10.5301/ejo.5000801>.
- [46] S. Kang, J. Kwon, C.J. Ahn, B. Esmali, G.B. Kim, N. Kim, H.S. Sa, Generation of customized orbital implant templates using 3-dimensional printing for orbital wall reconstruction, *Eye* 32 (2018) 1864–1870 <https://doi/10.1038/s41433-018-0193-1>.